Direct Comparison of Sea Surface Velocity Estimated From Sentinel-1 and TanDEM-X SAR Data

Anis Elyouncha, *Member, IEEE*, Leif E. B. Eriksson, *Member, IEEE*, and Harald Johnsen, *Member, IEEE*

***Abstract*—This article presents the first direct comparison of the sea surface radial velocity (RVL) derived from the two satellite SAR systems Sentinel-1 and TanDEM-X, operating at different frequencies and imaging modes. The RVL is derived from the Doppler centroid (Dc) provided in the Sentinel-1 OCN product and from the along-track interferometric phase of the TanDEM-X. The comparison is carried out using unique opportunistic acquisitions, collocated in space and time, over three different sites located in the Iceland Sea, the Pentland Firth, and the Kattegat Sea. First, it is observed that the RVL derived from both satellites is biased, thus calibration is applied using the land as a reference. The comparison shows that the correlation and the mean bias between the two datasets depend on the differences in acquisition time, incidence angle, and azimuth angle, and on wind and surface velocities. It is found that, given a time difference of $\lesssim$ 20 min, the spatial correlation coefficient is relatively high (between 0.70 and 0.93), which indicates that the two SAR systems observe similar sea surface current fields. The spatial correlation degrades primarily due to increasing time difference and decreasing velocity magnitudes. It is also found that the mean RVL bias increases primarily with the radial wind speed, which suggests that the bias is mainly due to the wave-induced Doppler shift. This article shows that under certain conditions, i.e., similar acquisition geometry and short time delay, a good agreement between the two independently derived RVL is achieved, both in the spatial variation and absolute mean value. This encourages a synergistic use of the sea surface velocity estimated from different C- and X-band SAR systems.**

***Index Terms*—Along-track interferometry (ATI), ocean surface currents, SAR Doppler centroid (Dc), Sentinel-1, TanDEM-X.**

I. Introduction

OCEAN surface circulation affects the weather, the climate, ship navigation, fish industry, oil spill, and plastic dispersion. Thus, ocean current observations are very important in a variety of applications [1]. In addition, ocean currents provide a potential source of renewable energy. For instance, a promising source of marine energy is tidal currents. Since the tidal power is directly related to the current velocity, direct measurements of current velocity are required for the estimation and assessment of tidal power [2]. *In situ* observations of ocean currents, such as moored buoys and drifters are sparse. Satellite altimeters, provide indirect (through sea level) coarse-resolution observations of the geostrophic component of surface currents and are limited near the coast by their large footprint. Ground-based high-frequency radars are limited by their spatial coverage to about 100 km from the coast. This coverage is significantly reduced in low salinity water bodies [3], [4], such as the Baltic Sea. Synthetic aperture radar (SAR) offers a good complement for 2-D mapping and monitoring of sea surface currents. These high resolution SAR measurements of surface currents are even more relevant in coastal areas, shelf seas, straits, and channels, where the ocean circulation is more complex and highly variable both spatially and temporally.

There are two major techniques for extracting ocean surface velocity from SAR data [5]: along-track interferometry (ATI) and the Doppler centroid anomaly (Dca) analysis. The retrieval of surface velocity from ATI-SAR data has been demonstrated in several articles, e.g., [6]–[8]. It has been shown that ATI-SAR is capable of providing high spatial resolution ($\sim$100 m) surface velocity maps very close to the coastline. The Dca method was first introduced in [9] and further demonstrated in [10] and [11]. The Dca method generates surface velocity at a spatial resolution of a few kilometers. Results of retrieving surface currents using ENVISAT/ASAR data have been reported in several works, e.g., [12] and [13].

However, Sentinel-1 Doppler data are still underused in oceanographic studies, mainly due to attitude issues resulting in unreliable geophysical Dc [14], [15]. This underuse is also due to the fact that the terrain observation by progressive scan (TOPS) imaging mode is the default acquisition mode over land, which is not optimal for ocean applications. In this mode, the azimuth steering of the antenna beam results in targets, at different azimuth positions, observed under different squint angles, i.e., Doppler centroids (Dcs) [16]. This induces a scalloping effect, i.e., periodic ramp-like signal, which adds to the geophysical signal [17]. This has a direct consequence on the retrieved geophysical velocity.

Consequently, the combination of TOPS mode and the attitude inaccuracy hinders the geophysical interpretation and extraction of ocean parameters, such as waves and currents. Recent updates of the level two processor, yielded an improvement in the geophysical Dc, and hence, promising results [15]. Yet, only few ocean studies have explored the Sentinel-1 data for ocean

Manuscript received December 25, 2021; revised February 18, 2022; accepted February 25, 2022. Date of publication March 9, 2022; date of current version March 29, 2022. This work was supported by the Swedish National Space Agency (SNSA) under Contract dnr 214/19. *(Corresponding author: Anis Elyouncha.)*

Anis Elyouncha is with the Department of Space, Earth and Environment, Chalmers University of Technology, 41296 Gothenburg, Sweden (e-mail: anis.elyouncha@chalmers.se).

Leif E. B. Eriksson is with the Department of Radio and Space Science, Chalmers University of Technology, SE-41296 Gothenburg, Sweden (e-mail: leif.eriksson@chalmers.se).

Harald Johnsen is with the Energy & Technology, NORCE Norwegian Research Centre AS, 5838 Tromso, Hordaland, Norway (e-mail: hjoh@norceresearch.no).

Digital Object Identifier 10.1109/JSTARS.2022.3158190

current retrieval, e.g., [18] and [19], compared to the wealth of data acquired by Sentinel-1 A and Sentinel-1B since 2014 and 2016, respectively.

The main limitation of a single satellite-borne SAR for monitoring geophysical processes and particularly fast evolving ocean dynamics, is the long revisit time. This revisit time can be reduced by combining overlapping swaths, but this is only possible at high latitudes. In order to overcome this limitation and enhance the temporal resolution of observations, data from several satellites should be combined. This raises the question of consistency between the datasets acquired by different platforms and the need for cross-calibration prior to synergistic use of observations. A first step toward cross-calibration is comparison, to identify possible biases and investigate their causes.

In this article, the sea surface velocity derived from the C-band Sentinel-1 SAR is compared to the velocity derived from the X-band ATI-SAR TanDEM-X. This is the first direct comparison of the sea surface velocity derived from two independent spaceborne SARs operating at different frequency bands (C- and X-band) and imaging modes (TOPS and stripmap).

II. Background

A. SAR-Observed Doppler Shift and Velocity

SAR measures the normalized radar cross section (NRCS), also called backscatter, and the Doppler frequency shift, also called Dc. The NRCS responds mainly to the surface roughness, thus over sea it is used to retrieve wind speed and wave height. The Doppler shift responds to the surface motion, thus can be used to infer the surface velocity. A single-beam SAR is only capable of measuring the radial component of the surface velocity (RVL, also called Doppler velocity). The Doppler shift (f_D) measured by SAR is related to the horizontal radial velocity (RVL) (U_D) by [9], [10], [20]

$$U_D = \pi f_D / k_e \sin\theta \tag{1}$$

where k_e is the electromagnetic wavenumber and θ is the incidence angle.

SAR observes the ocean velocity integrated vertically over the upper few-millimeters layer, horizontally over its resolution cell (few meters) and temporally over its integration time (few seconds). The radial sea surface velocity, i.e., the surface velocity projected on the radar ground range, U_D, can be decomposed into three components as follows [10]:

$$U_D = u_{cr} + c_B + c_o. \tag{2}$$

The first term is the surface current velocity projected on the ground range, i.e., $u_{cr} = u_c \cos\varphi_c$, where u_c is the surface current magnitude and φ_c is its angle relative to the line-of-sight. This term is independent of frequency and polarization but depends on the azimuth angle of the radar. The second term is due to the Bragg waves phase speed, which depends on the frequency, incidence angle, and azimuth angle. For instance, at an incidence angle of 30°, the Bragg wave phase speed is 31 cm/s and 25 cm/s for C-band and X-band, respectively. The last term is due to the orbital velocities of the long waves (at least three times longer than the Bragg waves). This term is dependent on frequency, polarization, incidence angle, and azimuth angle. The dependence of c_B and c_o on the azimuth angle is implicit. The full formulas of these two terms can be found in several references, e.g., [21]–[23]. The dependence on polarization is due to the fact that the orbital velocities are weighted by the backscatter, which depends on polarization. The orbital velocities contribution can be up to 1 m/s [9], [22]–[24], hence it is expected to be the dominant term in most cases.

The sea surface is dynamic, hence the time delay between acquisitions suitable for comparison is limited by the decorrelation time of the velocity field. Moreover, the RVL estimated from two different single-beam SARs can only be compared if the measurements are acquired, by the two SARs, with similar azimuth angles. This reduces further the number of acquisitions suitable for comparison. The NRCS can only be compared if it is measured with similar incidence and azimuth angles. Assuming a nominal right looking antenna (or if both platforms use zero Doppler steering) with line-of-sight perpendicular to the flight direction, the condition of similar azimuth angles corresponds to close satellite headings. Hereafter, the satellite heading is used as an indicator of azimuth angle similarity.

Finally, the difference between radial velocities estimated using two radars operating at different frequencies, e.g., Sentinel-1 and TanDEM-X, will be due to the last two terms in (2). This will be the case even if the current is constant and both sensors are well calibrated, i.e., excluding all instrument and processing biases. However, previous studies [23], [24] have shown that the RVL observed at C- and X-band (and even at Ka-band [22]) is comparable, i.e., within 0.2 m/s. To sum up, the discrepancy between the two sensors will depend on the temporal difference, the incidence and azimuth angles, and the wind speed and direction.

B. Effect of Radar Parameters and Wind Conditions on RVL

The RVL varies with the radar parameters, i.e., frequency, polarization, incidence angle, and azimuth angle, and with the environmental conditions of the sea surface, mainly wind speed and wind direction. The RVL shown in this section represents the last two terms of (2) representing the wave-induced velocity, i.e., the current is set to zero. These two components are more complicated to interpret than the current contribution. Fig. 1 shows the variation of the RVL as a function of incidence angle θ (left panel), wind speed u_{10} (middle panel), and relative wind direction φ (right panel). The curves were calculated using a semiempirical model proposed in [23].

First, it can be noted that the RVL is slightly higher at C-band than at X-band and it is higher at HH polarization than at VV polarization. The difference is small at low-to-moderate winds and becomes larger at high winds. Second, it can be observed that the RVL decreases with incidence angle and increases with wind speed. The variation of the RVL with relative wind direction follows a cosine-like curve. It is maximum (in magnitude) at upwind ($\varphi = 0$) and downwind ($\varphi = \pm 180$) and vanishes at the crosswind ($\varphi = \pm 90$). The RVL is positive when the sea surface is moving toward the radar and negative when it is moving away from the radar. Note that different authors may adopt different conventions of the RVL sign. Moreover, it can also be noticed

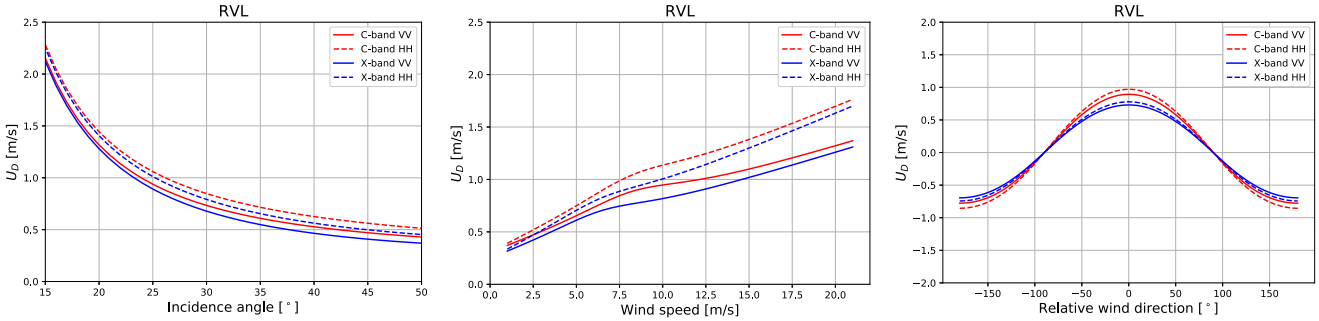

Fig. 1. Variation of the RVL with radar parameters and wind conditions. (a) As a function of θ for $u_{10} = 7$ m/s and $\varphi = 0°$. (b) As a function of u_{10} for $\theta = 30°$ and $\varphi = 0°$. (c) As a function of φ for $u_{10} = 7$ m/s and $\theta = 30°$. θ is the incidence angle, u_{10} is the wind speed at 10 m height and φ is the relative wind direction, i.e., difference between wind direction and SAR line of sight. Upwind is $\varphi = 0°$, downwind is $\varphi = \pm 180°$ and crosswind is $\varphi = \pm 90°$.

that the RVL is asymmetric in wind direction, i.e., slightly larger (in magnitude) at upwind than at downwind.

III. Datasets

A. Sentinel-1 Data

This work is based on the data provided in the Sentinel-1 level 2 ocean (OCN) product in interferometric wide (IW) swath mode [25]. The IW mode combines three subswaths (IW1, IW2, and IW3). The total swath is 250 km wide. Only the IW swath that overlaps with TanDEM-X acquisition is extracted. The OCN product contains three components: ocean wind field (OWI), ocean swell (OSW), and RVL. The OSW component is not available for IW mode. The OWI component is a gridded estimate of wind speed and direction at ten meters height. The RVL component contains mainly the Dc and the RVL [25]. The spatial resolution of the OWI and RVL components is $\sim 1 \times 1$ km. The center frequency of Sentinel-1 SAR is 5.405 GHz and the polarization of all the acquisitions used here is VV.

B. TanDEM-X Data

TanDEM-X is a system of two satellites flying in tandem and carrying almost identical X-band SAR sensors [26]. The images used here are part of the coregistered single-look complex (SLC) dataset. These images are acquired with the stripmap bistatic mode. The scene size of each acquisition is approximately 50 km in azimuth and 30 km in range. The raw resolutions of the SLC data are $\sim$2.14 and $\sim$3.29 m in ground range and azimuth, respectively. The center frequency of TanDEM-X SAR is 9.649 GHz and the polarization of all the acquisitions used here is VV.

C. Wind and Current Model Data

Wind data are obtained from the ERA5 reanalysis product provided by the European Centre for Medium-Range Weather Forecasts (ECMWF). ERA5 provides hourly estimates on a 31-km grid (https://confluence.ecmwf.int/display/CKB/ERA5%3A+data+documentation). The surface current data are obtained from the Copernicus Marine Service (https://marine.copernicus.eu/) and the Swedish Meteorological and Hydrological Institute (SMHI). The surface currents provided by the circulation models used here correspond to the depth at one meter. The vertical thickness of the model grid at the surface is one meter.

D. Data Selection

The criteria for data selection are spatial overlap between acquisition for the direct comparison, time difference below 30 min and heading difference below 5°. The 30-min time difference is a classical threshold used when comparing satellite-radar data to *in situ* measurements [27]. In addition, the TanDEM-X acquisitions are required to have an along-track baseline smaller than 100 m and average coherence larger than 0.5 over sea. We have selected six acquisitions, two in the Iceland Sea, two in the Pentland Firth, and two in the Kattegat Sea (Fehmarn Belt). The Sentinel-1 satellite scene frames are shown in Fig. 2.

The selected satellite images used for the comparison are all acquired in the ascending pass, i.e., heading$\sim 350°$. The most important acquisition parameters for this study, i.e., time, heading angle, and incidence angle, and for the three test areas are given in Table I.

IV. RVL Estimation

A. RVL Estimation From Sentinel-1

For Sentinel-1, the SLC-to-Doppler shift processing is performed by the S1-IPF Level 2 processor and provided in the S1 OCN RVL product. In addition to the total observed Doppler shift, the OCN product contains the geometric and miss-pointing Dc. The geometric Dc is due to the satellite velocity relative to the solid rotating earth, hence a dependence on the satellite attitude. The miss-pointing Dc is due to the antenna pattern skewness as a function of elevation angle.

In general, the total observed Dc (f_{Dc}) can be decomposed into the following components [15]:

$$f_{\mathrm{Dc}} = f_{\mathrm{geo}} + f_{\mathrm{miss}} + f_{\mathrm{scal}} + f_{\mathrm{phys}} + f_{\mathrm{bias}} \tag{3}$$

where f_{geo} is the geometrical Dc term, f_{miss} is the antenna miss-pointing term, f_{scal} is the scalloping signal term (discussed later), $f_{\mathrm{phys}} = f_{\mathrm{curr}} + f_{\mathrm{wave}}$, also called the Dca, is the sum of the current and wave induced Dc. f_{bias} groups all unknown errors,

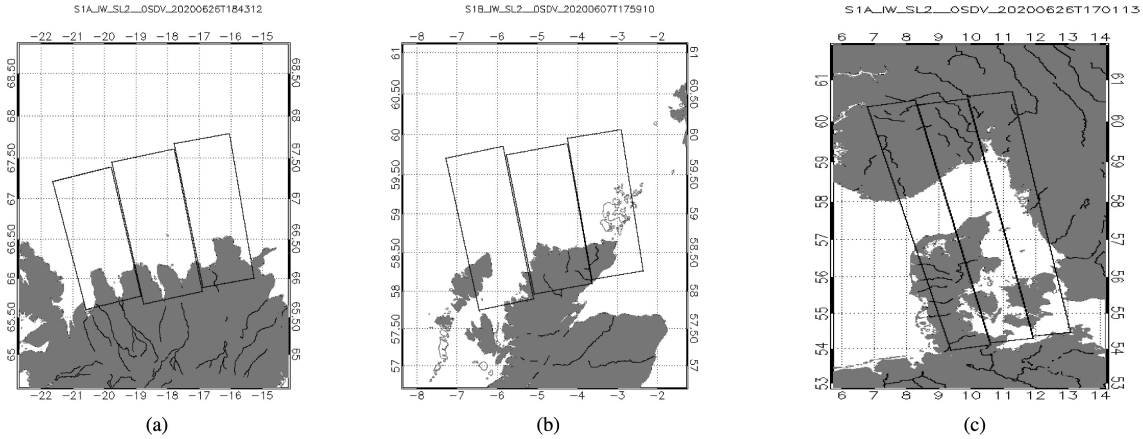

Fig. 2. Geographical locations of the selected data. (a) Iceland Sea. (b) Pentland Firth. (c) Kattegat Sea. The black frames represent the three swaths (1, 2, and 3 from left to right) of the Sentinel-1 IW mode. The TanDEM-X overlaps with Sentinel-1 in the first swath in the Iceland Sea, in the third swath in the Pentland Firth, and in the second swath in the Kattegat Sea. The Fehmarn Belt is located in the southern part of the middle swath.

TABLE I
SATELLITE ACQUISITION PARAMETERS

Iceland Sea			
Satellite	Acquisition time [UTC]	Heading angle [deg]	Incidence angle [deg]
Sentinel-1A	2020-06-26 18:43:43	346.302	33.368
TanDEM-X	2020-06-26 18:40:42	346.373	33.79
Sentinel-1A	2020-07-18 18:59:36	349.929	43.445
TanDEM-X	2020-07-18 18:40:45	346.373	33.788
Pentland Firth			
Satellite	Acquisition time [UTC]	Heading angle [deg]	Incidence angle [deg]
Sentinel-1B	2020-06-07 17:59:14	349.267	43.469
TanDEM-X	2020-06-07 17:47:01	348.156	33.23
Sentinel-1A	2020-06-13 17:59:38	350.659	43.538
TanDEM-X	2020-06-13 17:38:26	346.275	21.454
Fehmarn Belt			
Satellite	Acquisition time [UTC]	Heading angle [deg]	Incidence angle [deg]
Sentinel-1A	2020-06-26 17:03:01	349.557	38.850
TanDEM-X	2020-06-26 17:02:44	350.630	44.56
Sentinel-1A	2020-07-08 17:01:14	349.557	38.850
TanDEM-X	2020-07-08 16:45:44	347.103	21.439

e.g., temperature compensation applied to the antenna during data take. See [15] and [28] for more details about these terms.

In order to retrieve the geophysical surface velocity, the nongeophysical terms must be removed

$$f_{\text{phys}} = f_{\text{Dc}} - f_{\text{geo}} - f_{\text{miss}} - f_{\text{scal}} - f_{\text{bias}}. \tag{4}$$

The correction for the geometric and miss-pointing Dc is based on the information provided in the OCN product (*rvlDcGeo* and *rvlDcMiss*). f_{bias} is removed by calibration. The correction of the scalloping signal is discussed hereafter. The RVL is derived from the estimated Dca as [29]

$$U_D = \frac{\lambda_C \, f_{\text{Dca}}}{2 \sin \theta} \tag{5}$$

where λ_C is the C-band electromagnetic wavelength for Sentinel-1.

Fig. 3 (left panel) shows the measured Dc by Sentinel-1 A over the Iceland Sea. Note the striping effect along the azimuth direction. This effect is due to the scalloping signal mentioned earlier. This is not a physical signal but an artifact that hinders the analysis of the spatial variation of the Dc and consequently the surface velocity, thus it should be corrected. The right panel of Fig. 3 shows the central part of the azimuth cut (through the center) of the magnitude of the Fourier transform of the Dc image. The spectrum is interpolated by a factor four to improve the visibility. It can be seen that, as expected, the scalloping signal has a dominant frequency and several harmonics of decreasing amplitude. Given the very small amplitude of these harmonics, it is difficult to detect accurately their location and compensate them individually. Therefore, all the frequencies higher than the first harmonic are filtered out. The spatial scale of ocean currents is about a few kilometers, hence most of the geophysical information is contained in the main beam and the higher frequencies contain the scalloping signal and noise. The middle panel of Fig. 3 shows the Dc after descalloping. It can be observed that the scalloping signal (striping effect) and noise are removed while the low-frequency geophysical signal is preserved.

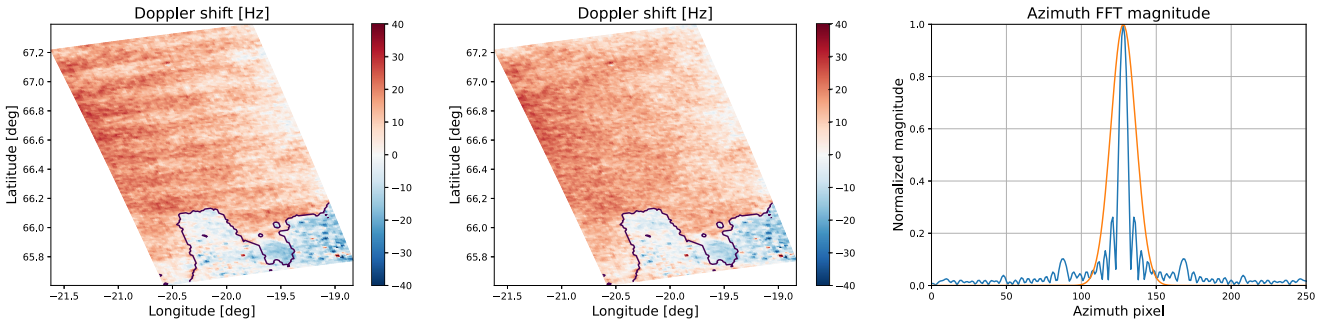

(a) (b) (c)

Fig. 3. Removal of the scalloping effect, Sentinel-1 A, 2020-06-26, Iceland Sea. (a) Before descalloping. (b) After descalloping. (c) A cut through the center along the azimuth direction of the power spectrum (blue curve) and the Gaussian window (red curve) used to filter the scalloping signal. The spectrum is zero padded by a factor four to improve the visibility.

B. RVL Estimation From TanDEM-X

For TanDEM-X, first, the interferogram is formed using the two SLC coregistered images. TanDEM-X is not a pure along-track interferometric system, but a hybrid (across- and along-track) interferometric SAR. Thus, the observed phase is sensitive to both topography and displacement. Assuming the baseline and surface displacement are small compared to the range, the observed phase can be decomposed as [30]

$$\phi_{\text{observed}} = \phi_{\text{topo}} + \phi_{\text{disp}} + \phi_{\text{atmos}} + \phi_{\text{error}} + 2n\pi \tag{6}$$

where ϕ_{topo} is the topographic phase, ϕ_{disp} is the displacement phase, ϕ_{atmos} is the phase due to atmospheric delay, n is an integer and ϕ_{error} groups all type of systematic errors (bias) and random errors (noise). All contributions other than the displacement (ϕ_{disp}) must be removed. The atmospheric phase is negligible given the very small time delays, between the two SLCs, considered here ($\lesssim$ 5 ms). The topographic phase is removed using a geoid and a digital elevation model (DEM). Here, the EGM2008 (https://earth-info.nga.mil/) and the Copernicus DEM called COP-DEM_GLO-90 (https://spacedata.copernicus.eu/web/cscda/dataset-details?articleId=394198) are used. To reduce the phase noise and increase the phase precision, the interferogram is multilooked, which downgrades the spatial resolution. The multilooked pixel size is about 100 m in ground range and azimuth. At this stage the interferometric phase is ambiguous and only known within 2π. In order to be able to relate the interferometric phase to velocity, the phase must first be unwrapped. Once the interferogram is unwrapped, velocity values can be derived. The estimation of the RVL from ϕ_{disp} is given by [29]

$$U_D = \frac{\lambda_X \phi_{\text{disp}}}{4\pi\tau \sin\theta} \tag{7}$$

where λ_X is the X-band electromagnetic wavelength, τ is the interferometric time delay. Note, that in (5) and (7), the vertical component of the sea surface velocity is neglected.

Finally, it was found that both the velocity estimated from Sentinel-1 and TanDEM-X are biased, i.e., nonzero over land, and varies with elevation angle (range). The estimated velocity is calibrated using land as a reference. The bias estimated over land is applied to the velocity over sea.

V. Results

In the comparisons presented hereafter, the high resolution TanDEM-X data are resampled to the coarser Sentinel-1 grid. The TanDEM-X images are, however, presented in their multilooked resolution, i.e., $\sim$100 m. The convention adopted here is that positive and negative velocity means surface moving toward and away from the radar, respectively. Since all the analyzed SAR images are acquired in ascending passes with the SAR antenna looking to the right of the flight direction, positive velocity means flow moving from East to West and vice-versa. In the following, the discrepancy between Sentinel-1 and TanDEM-X data is indicated by the correlation coefficient (R), the mean absolute error (MAE), and the root mean squared error (RMSE). The spatial correlation is affected by the time delay between the collocated data, the difference in the acquisition geometry (incidence and azimuth angles) and the signal-to-noise ratio (SNR). The SNR in this context refers to the ratio of the mean magnitude of the observed RVL to its standard deviation. Model wind and current fields, interpolated to SAR grid, are also shown to analyze the effect of the winds and currents on the RVL correlation and bias. The results of the RVL comparison corresponding to each region are discussed in more detail in separate sections.

A. Iceland Sea

Fig. 4 shows the model wind field over the area covered by the SAR image on 2020-06-26 (upper panel) and 2020-07-18 (lower panel). In both acquisitions, the wind is nearly northerly, i.e., nearly cross-wind relative to the SAR-look direction. In the lower part of the first acquisition, the wind is turning toward the west, i.e., toward upwind. As mentioned above, the RVL is minimum in magnitude in the cross-wind direction. In the first acquisition the incidence and azimuth angles, of Sentinel-1 and TanDEM-X, are almost identical (see Table I), thus the NRCS can also be compared. Fig. 5 shows the NRCS measured by Sentinel-1 A (left panel), TanDEM-X (middle panel), and the scatterplot (right panel). The spatial similarity is clearly noticeable from the images and confirmed by the high correlation coefficient (0.82). The MAE and RMSE are both approximately 1 dB, which might be due to instrument calibration. Note that the model wind, for the first acquisition, does not resolve the sharp

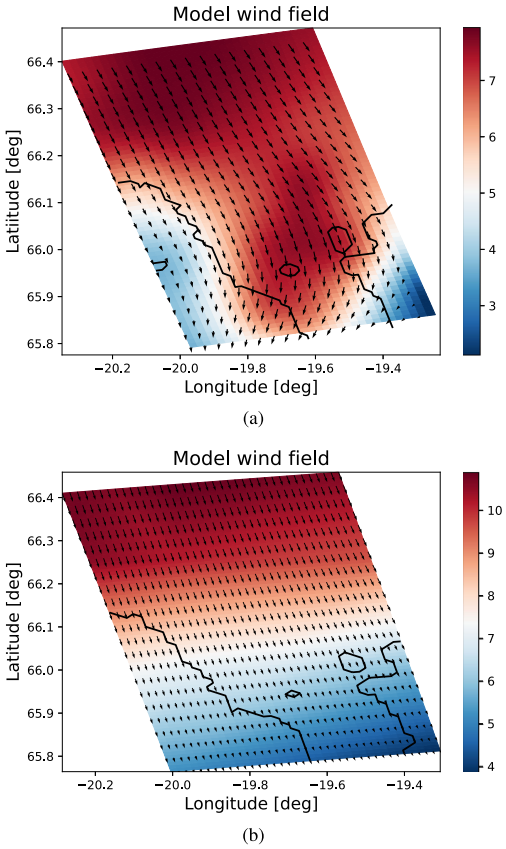

Fig. 4. Model wind field (ECMWF) over the Iceland Sea on 2020-06-26 (panel a) and 2020-07-18 (panel b). The colormap represents the wind speed and the arrows represent the wind vectors.

front observed in the NRCS image. It shows, however, a gradual turning of the wind vectors to the west from the top to bottom of the image (see Fig. 4). Relative to the satellite's line-of-sight this corresponds to cross-wind and near upwind in the upper and lower part of the image, respectively. This explains the higher NRCS values in the lower part compared to the upper part of the image shown in Fig. 5.

The estimated RVL is shown in Fig. 6. In the first acquisition (upper row), the spatial patterns detected by the two sensors are very similar despite the difference in the spatial resolution. Quantitatively, the correlation coefficient is very high (0.93), which is mainly due to the short time separation ($\sim$3 min) between the Sentinel-1 and TanDEM-X passes. The scatterplot shows two clusters (negative and positive) indicating two flows of one moving toward and one moving away from the SAR. For the second acquisition (lower row), however, the correlation is very poor (0.23), which is mainly due the large time difference between the Sentinel-1 and TanDEM-X passes ($\sim$20 min). Note also the low velocity values ($\leq$ 0.5 m/s), i.e., low SNR, which might contribute to the decorrelation. The MAE and RMSE for the two acquisitions are small (between 0.1 and 0.25 m/s) due to the low contribution of the cross-wind to the observed Doppler shift. No current measurements were available at the location and time of the satellite acquisitions to validate these observations. Finally, note the similarity between the NRCS and velocity maps (see Fig. 6). This is expected since both the NRCS and Dc are affected by the waves and currents, e.g., both increase with wind speed.

B. Pentland Firth

The Pentland Firth is characterized by one of the strongest and most energetic tidal streams in the world [31]. Fig. 7 (left column) shows the model wind field over the area covered by the SAR image on 2020-06-07 (upper panel) and 2020-06-13 (lower panel). The wind speed is moderate and low during the first and second satellite acquisitions, respectively. The wind direction is northerly (cross-wind) during the first acquisition and south-easterly ($\sim 45^\circ$ relative to the SAR line-of-sight) during the second acquisition. Therefore, the wind is expected to have a minimum contribution in the first case and moderate (due to low wind speed) contribution in the second case. This is confirmed by the very small (0.09) and small (0.3) MAE indicated in Fig. 8.

Fig. 7 (right column) shows the sea surface current field provided by the ocean circulation model. These model data are provided in a product called NORTHWEST-SHELF_ANALYSIS_FORECAST_PHY_004_013 [32] provided by the Copernicus marine service. The horizontal grid spacing is 1.5 km covering the entire North-West European Shelf. For the first acquisition (upper panel), the model current field shows a clear and strong tidal stream from east to west (Ebb tide). The current speed in the core of the stream, located in the center of the image, reaches 2.5 m/s. For the second acquisition (lower panel), the model current field shows also a clear tidal stream from west to east (Flood tide). It can be noticed that the current speed of the flood tide is lower than the Ebb tide. Moreover, the region of the strongest stream is displaced from west to south-east during the flood tide.

Fig. 8 (upper row) shows the RVL derived from Sentinel-1B (left panel) and TanDEM-X (right panel) on 2020-06-07. Despite the difference in frequency and spatial resolution, the two sensors observe similar circulation patterns. This pattern is very similar to the current field predicted by the ocean model shown in Fig. 7, but with additional small scale details resolved by SAR. The main feature in the circulation is the strong Ebb tidal stream flowing out of the North Sea, i.e., from east to west. There is a good agreement between the magnitude of the two retrieved velocities, with RVL in the core of the tidal stream exceeding 2 m/s, although the values differ slightly in some other areas. The quantitative comparison is shown in the right panel of Fig. 8. The high spatial correlation coefficient (0.86) suggests that two sensors observe similar current field. The MAE and the RMSE are small (0.09 and 0.4), owing to the favorable wind direction (cross-wind).

The RVL derived from Sentinel-1 A (left panel) and TanDEM-X (right panel) during the second acquisition (2020-06-13) is shown in Fig. 8 (lower row). In this case, the spatial correlation is low (0.51) owing to the large time difference between the two satellite passes ($\sim$21 min). The current magnitude is also lower than the first case, hence the lower SNR and lower correlation. The MAE (0.31 m/s) is larger than the first acquisition because of the nearly upwind direction, i.e., additional wave-induced Doppler shift. Finally, it is worth noting that the asymmetry

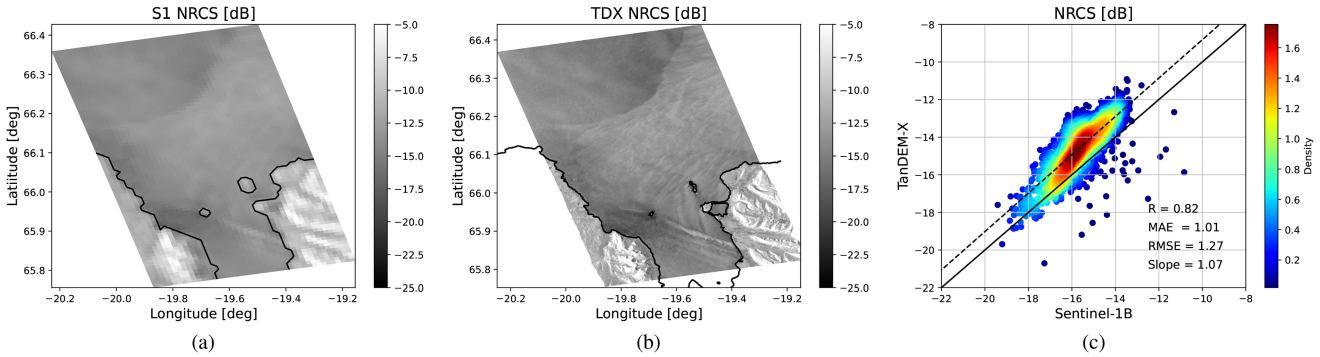

Fig. 5. Comparison of the NRCS (in dB) measured by Sentinel-1 and TanDEM-X over the Iceland Sea on 2020-06-26 18.00. (a) Sentinel-1 NRCS. (b) TanDEM-X NRCS. (c) Scatter plot. R, MAE, and RMSE.

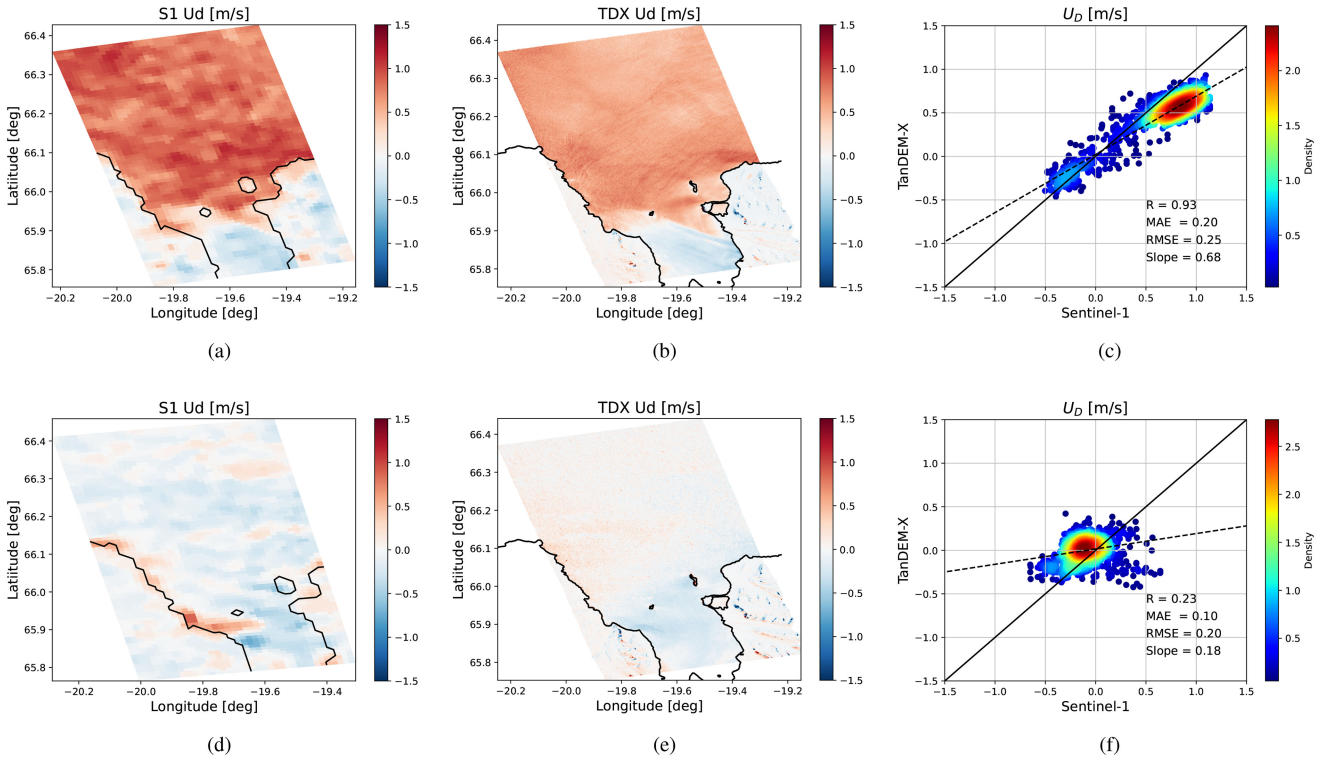

Fig. 6. Comparison of the surface RVL (in m/s) derived from Sentinel-1 and TanDEM-X over the Iceland Sea on 2020-06-26 (upper row) and 2020-07-18 (lower row). (a, d) Sentinel-1 RVL. (b, e) TanDEM-X RVL. (c, f) Scatter plot.

in the tidal stream structure, e.g., shift of the core toward the east, between the flood and Ebb is in agreement with the model data shown in Fig. 7. The displacement of the core of the tidal stream out of the area imaged by SAR explains the low-velocity magnitude observed during the flood (second) acquisition.

C. Fehmarn Belt (Kattegat Sea)

The Fehmarn Belt is an important channel for the exchange of water between the Baltic Sea and the North Sea. Fig. 9 shows the model wind and current fields in the Fehmarn Belt provided by SMHI. The wind field is derived, by SMHI, from the Arome and ECMWF models. The current filed is derived from the NEMO-Nordic model. During the first acquisition (2020-06-26, upper row), the wind speed is ∼5 m/s dominantly westward, i.e., upwind relative to SAR line-of-sight. The current is flowing from east to west, i.e., flowing out of the Baltic Sea into the Kattegat Sea, in the area covered by the satellite image (see Fig. 10). During the second acquisition (2020-07-08, lower row), the wind is stronger (∼8 m/s) dominantly south-eastward, i.e., nearly downwind relative to SAR line-of-sight. The current flowing from west to east, i.e., flowing from the Kattegat Sea into the Baltic Sea, in the area covered by the satellite image. Thus according to our convention, the estimated velocity is expected to be dominantly positive and negative in the first and second acquisitions, respectively.

Fig. 10 shows the estimated velocity from Sentinel-1 A (left) and TanDEM-X (middle), for the first acquisition (upper row) and second acquisition (lower row). Despite the difference in resolution, the images observed by the two satellites exhibit

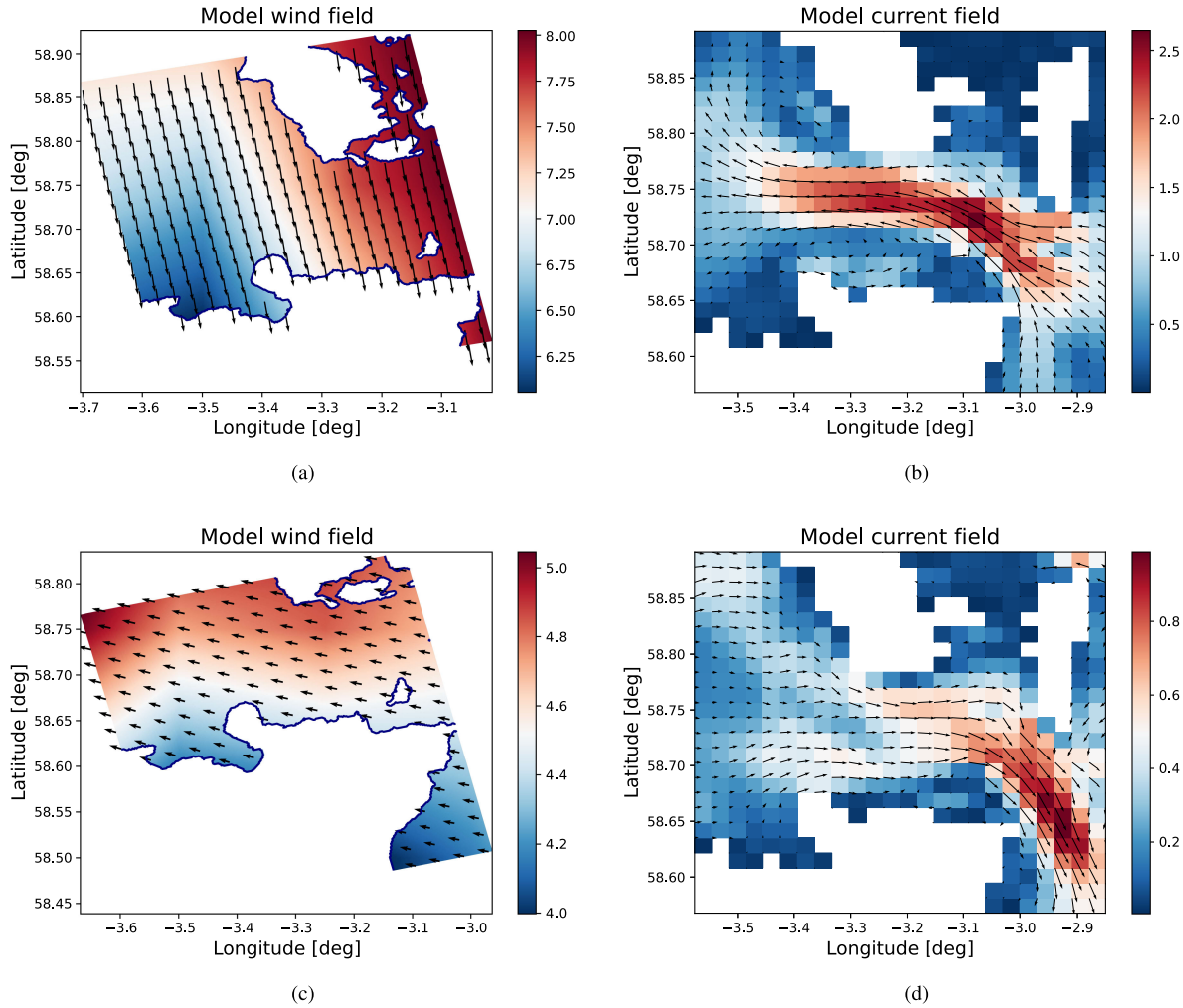

Fig. 7. Model wind field (ECMWF) and current field (FOAM), 2020-06-07 (upper row), 2020-06-13 (lower row). (a, c) Wind. (b, d) Current. The colormap represents the wind and current speed in m/s and the arrows represent the wind and current vectors.

TABLE II
SUMMARY OF THE COMPARISON RESULTS AND RELEVANT ACQUISITION PARAMETERS

	Iceland Sea 1	Iceland Sea 2	Pentland Firth 1	Pentland Firth 2	Fehmarn Belt 1	Fehmarn Belt 2
R	0.93	0.25	0.86	0.51	0.71	0.71
MAE	0.20	0.10	0.09	0.31	0.88	0.97
RMSE	0.25	0.18	0.44	0.46	0.93	1.01
Incidence (S1 - TDX) [deg]	33.37 - 33.79	43.44 - 33.78	43.47 - 33.23	43.53 - 21.45	38.85 - 44.56	38.85 - 21.44
Incidence difference [deg]	0.42	9.66	10.24	22.08	5.71	17.41
Heading difference [deg]	0.07	3.53	1.11	4.38	1.073	2.45
Time difference [mm:ss]	3:01	19:00	12:13	21:12	1:43	15:02
Radial wind speed [m/s]	-1.17	-1.50	0.060	4.24	5.96	-6.30

similar spatial features, which are likely generated by the bottom topography. The scatterplots indicate a relatively high spatial correlation (∼0.7) between the velocity estimated from the two satellites. The MAE and RMSE, are large (∼1 m/s) compared to other regions (Iceland Sea and Pentland Firth). This is probably due to the wave-induced Doppler shift mentioned earlier, enhanced by the upwind and quasi downwind directions in the first and second acquisitions, respectively. The MAE in the first acquisition (∼0.88 m/s) and second acquisition (∼0.97 m/s) are in agreement with the stronger wind speed during the second acquisition (see Fig. 9). It is also worth noting the asymmetry in the spatial structure between the inflow and the outflow, possibly due to a change in stratification.

VI. DISCUSSION

Table II summarizes the results of the comparisons and the corresponding most relevant acquisition parameters. First, recall that the surface current-induced Doppler velocity is independent of the sensor and acquisition parameters. Thus in the presence

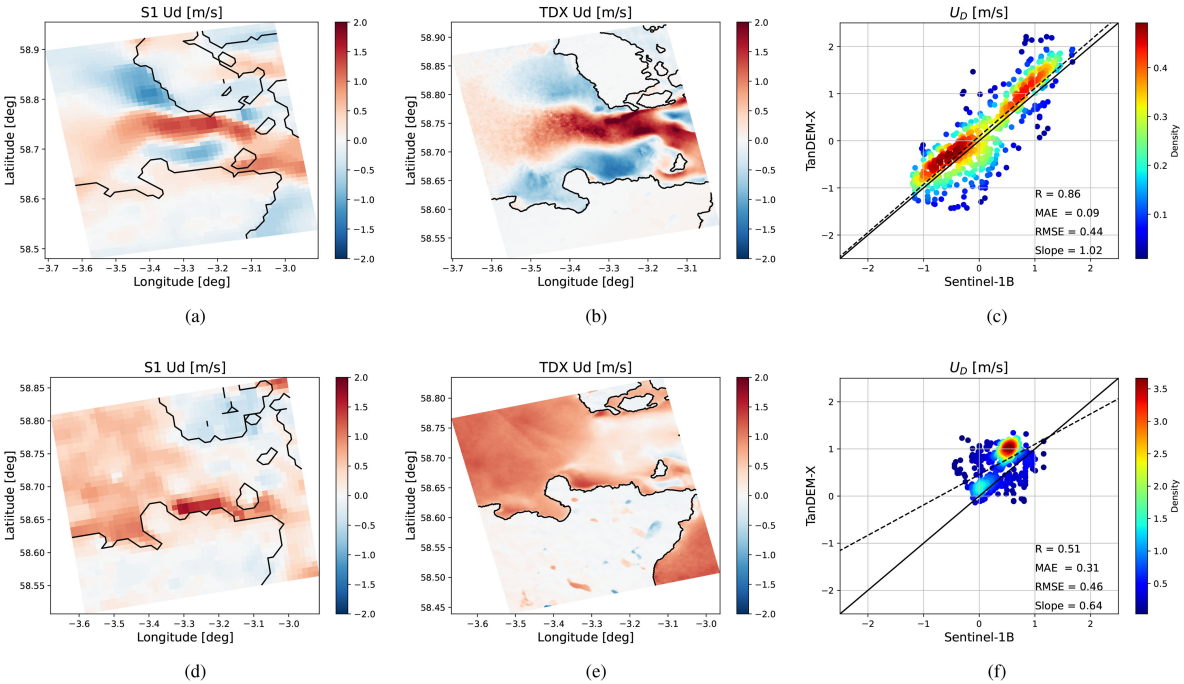

Fig. 8. Comparison of the surface RVL (in m/s) derived from Sentinel-1 and TanDEM-X over the Pentland Firth on 2020-06-07 (upper row) and 2020-06-13 (lower row). (a, d) Sentinel-1 RVL. (b, e) TanDEM-X RVL. (c, f) Scatter plot.

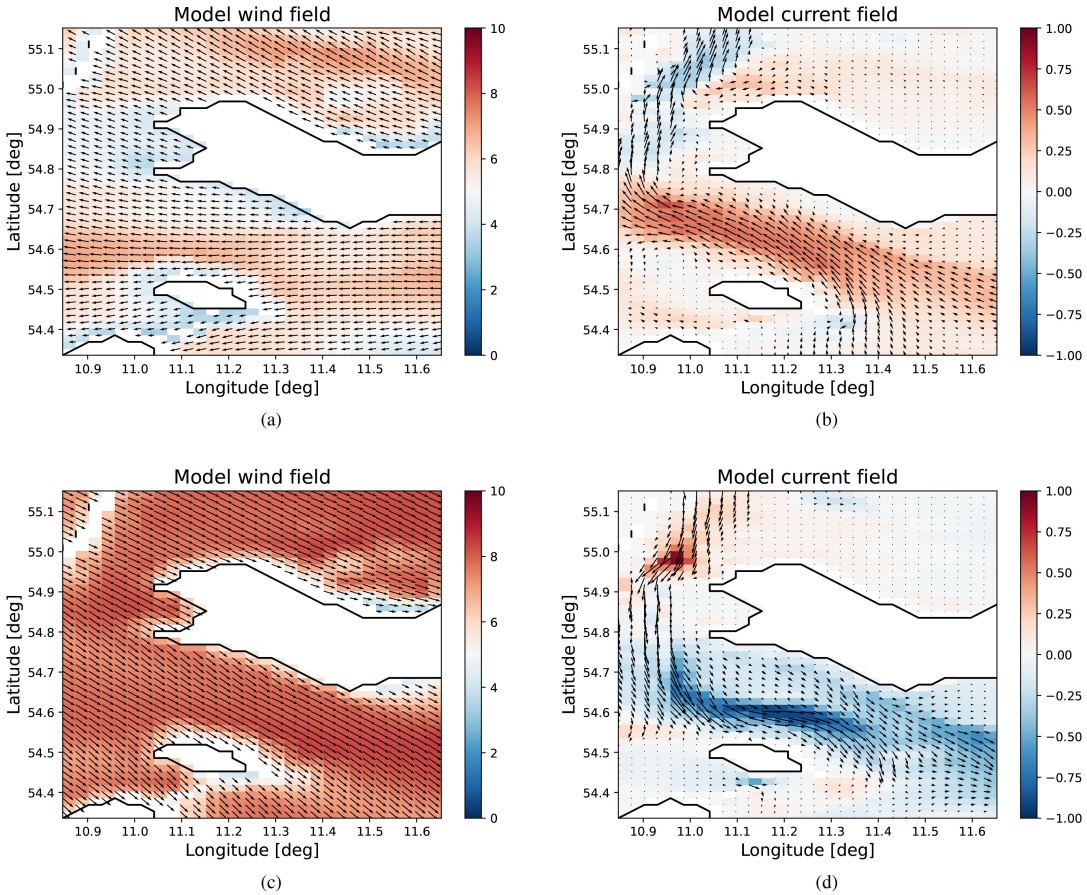

Fig. 9. Model wind (ECMWF and Arome) and current field (NEMO-Nordic), 2020-06-26 (upper row) 2020-07-08 (lower row), Fehmarn Belt (Kattegat Sea). (a, c) Wind. (b, d) Current. The colormap represents the wind speed and current vector projected on the satellite line-of-sight (in m/s) and the arrows represent the wind and current vectors.

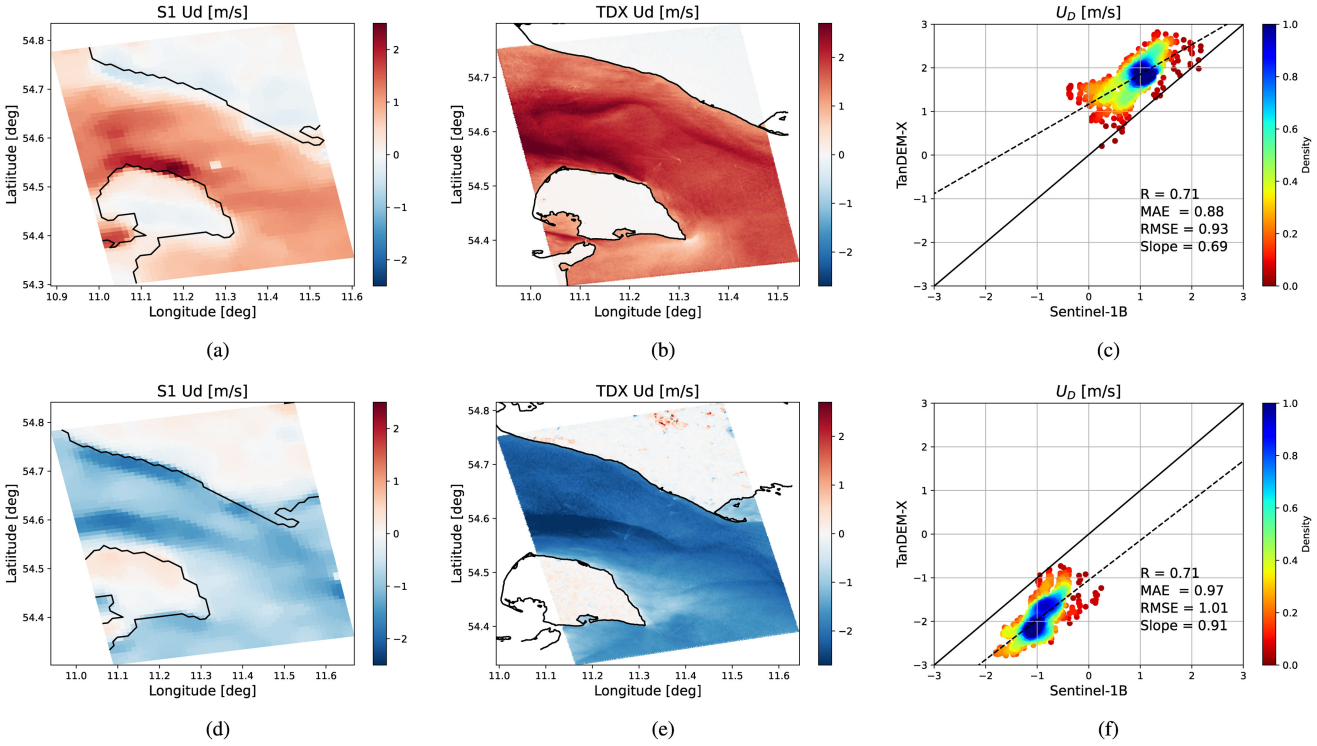

Fig. 10. Comparison of the surface RVL (in m/s) derived from Sentinel-1 and TanDEM-X over the Fehmarn Belt (Kattegat Sea) on 2020-06-26 (upper row) and 2020-07-08 (lower row). (a, d) Sentinel-1 RVL. (b, e) TanDEM-X RVL. (c, f) Scatter plot.

of a surface current only and in absence of waves the two sensors should measure the same Dc. The wave-induced Doppler velocity, however, depends on wind speed, relative wind direction, incidence angle, frequency, and polarization [9], [23], [33]. Since all the images used here are acquired with the same polarization (VV), the latter is not discussed further. It has been shown [9], [10], [23], [33] that the magnitude of the wave-induced Doppler velocity increases with increasing magnitude of the radial wind speed. The radial wind speed, i.e., the projection of the wind vector on the SAR line-of-sight, which takes into account the effects of both wind speed and relative wind direction, is given in the last row of Table II. It has been also shown that the magnitude of the wave-induced Doppler velocity decreases with incidence angle [23], [33]. The discrepancy between the two sensors in the observed velocity field is manifested as a change in the mean velocity or a change in the spatial distribution or both. The mean bias is expected to depend on the radial wind speed, to the highest degree, and on incidence and azimuth angles differences to lower degree. The change in spatial distribution is due to decorrelation. The spatial decorrelation is affected by the time difference, to the highest degree; the SNR, incidence, and azimuth angles differences to a lower degree. Note that, there might be conflicting effect of these parameters, e.g., low radial wind speed and large incidence-angle difference. Moreover, since the satellite acquisitions cover regions characterized by very different atmospheric and oceanic circulations, the bias and correlation will also depend on the temporal and spatial scales of the wind and current in these regions.

Table II shows that the first acquisition over the Iceland Sea gives the highest correlation coefficient (0.93). This is primarily due to the small time delay, and small incidence and heading angles differences. The second acquisition over the Iceland Sea gives the lowest correlation coefficient (0.25), primarily due to the large time delay (∼20 min), low SNR, and relatively large incidence and heading angles differences.

The first acquisition of Pentland Firth (2020-06-07) yields the second highest correlation coefficient (0.86). The time difference (12 min) gives slightly lower correlation than the first Iceland Sea case. Note that in this case the acquisition covers a strong Ebb tidal current (high SNR), which might explain the high correlation despite the time difference. In terms of bias, the cross-wind direction (see Fig. 7) gives the lowest radial wind speed, which yields the lowest wave-induced Doppler velocity. The second acquisition of Pentland Firth (2020-07-08) gives a low correlation coefficient (0.51), which is very likely due to the largest time difference (21 min), the largest incidence angle difference (22°), and the largest heading difference (4.4°).

The two acquisitions over the Fehmarn Belt give the largest RVL MAE and RMSE. In agreement with the largest magnitude of the radial wind speed, which yields the largest wave-induced Doppler velocity. The correlation coefficient is, however, still good (0.71) owing to the relatively small time difference, particularly in the first acquisition and high SNR in both acquisitions.

The results outlined in Table II suggest that the mean bias increases, primarily, with increasing radial wind speed, which implies that it is mainly due to the wave-induced Doppler contribution. The spatial correlation generally deteriorates with

increasing time difference and decreasing SNR. To summarize, the results suggest that the spatial correlation is primarily affected by the time difference between satellite passes, while the mean bias is mainly affected by the wind conditions, specifically the radial wind speed.

VII. Conclusion

A direct comparison of the sea surface RVL derived from two independent SAR systems (Sentinel-1 and TanDEM-X), operating at different frequency bands (C- and X-band), and imaging modes (Stripmap and IW), was performed. The comparison was carried out using unique opportunistic overlapping scenes of the two satellites over three different geographical locations, the Iceland Sea, the Kattegat Sea, and the Pentland Firth strait.

It was found that both datasets require calibration. After calibration using land as a reference, the radial velocities derived from the two systems compare qualitatively and quantitatively well. A high spatial correlation (up to 0.93) suggested that the two sensors observe similar ocean surface current fields. This correlation deteriorated with the time delay between acquisitions, but remained above 0.7 up to 15 min difference. When the time difference exceeded 15 min the correlation coefficients dropped to below 0.5. It is also noted that the SNR affected the correlation such that weak currents tend to decorrelate more rapidly than strong currents. Moreover, the mean bias increased, primarily, with increasing radial wind speed suggesting that the wave-induced Doppler velocity is the most plausible explanation for the RVL bias.

Assuming more collocated satellite acquisitions can be acquired in the future and development of accurate wave-induced Doppler models, it will be possible to correct for the wave-induced RVL. This study indicates that it is possible to combine data from C- and X-band SARs, to increase the spatial coverage and the temporal sampling in order to generate blended products of sea-surface velocity, which are needed in many ocean applications. Finally, it would be of interest to compare the SAR-derived RVL against *in situ* measurements from buoys and/or coastal radars. This is left for future work.

Acknowledgment

The authors would also like to thank the European Space Agency (ESA) and the German Aerospace Center (DLR) for providing Data for Sentinel-1 and TanDEM-X, respectively. The authors would also like to thank the European Centre for Medium Range Weather Forecasts (ECMWF), the Copernicus Marine Service (CMEMS), and the Swedish Meteorological and Hydrological Institute (SMHI) for providing the model data for wind and current fields. Finally, the authors thank the Swedish National Space Agency for funding this work.

References

[1] J. Röhrs *et al.*, "Surface currents in operational oceanography: Key applications, mechanisms, and methods," *J. Oper. Oceanogr.*, pp. 1–29, 2021.

[2] C. Garrett and P. Cummins, "The power potential of tidal currents in channels," *Proc. Roy. Soc. A, Math., Phys. Eng. Sci.*, vol. 461, no. 2060, pp. 2563–2572, 2005.

[3] K.-W. Gurgel, H.-H. Essen, and S. Kingsley, "High-frequency radars: Physical limitations and recent developments," *Coastal Eng.*, vol. 37, no. 3, pp. 201–218, 1999.

[4] C. Mantovani *et al.*, "Best practices on high frequency radar deployment and operation for ocean current measurement," *Front. Mar. Sci.*, vol. 7, p. 210, 2020.

[5] R. Romeiser *et al.*, *Direct Surface Current Field Imaging From Space by Along-Track InSAR and Conventional SAR*. Berlin, Germany: Springer, Feb. 2010, ch. 5, pp. 73–91.

[6] R. Goldstein and H. Zebker, "Interferometric radar measurement of ocean surface currents," *Nature*, vol. 328, pp. 707–709, 1987.

[7] R. Romeiser, H. Runge, S. Suchandt, R. Kahle, C. Rossi, and P. S. Bell, "Quality assessment of surface current fields from TerraSAR-X and TanDEM-X along-track interferometry and Doppler centroid analysis," *IEEE Trans. Geosci. Remote Sens.*, vol. 52, no. 5, pp. 2759–2772, May 2014.

[8] A. Elyouncha, L. E. B. Eriksson, R. Romeiser, and L. M. H. Ulander, "Measurements of sea surface currents in the Baltic Sea region using spaceborne along-track InSAR," *IEEE Trans. Geosci. Remote Sens.*, vol. 57, no. 11, pp. 8584–8599, Nov. 2019.

[9] B. Chapron, F. Collard, and F. Ardhuin, "Direct measurements of ocean surface velocity from space: Interpretation and validation," *J. Geophys. Res.*, vol. 110, Mar. 2005, Art. no. C07008.

[10] J. A. Johannessen *et al.*, "Direct ocean surface velocity measurements from space: Improved quantitative interpretation of Envisat ASAR observations," *Geophys. Res. Lett.*, vol. 35, no. 22, 2008, Art. no. L22608.

[11] M. W. Hansen, F. Collard, K. F. Dagestad, J. A. Johannessen, P. Fabry, and B. Chapron, "Retrieval of sea surface range velocities from Envisat ASAR Doppler centroid measurements," *IEEE Trans. Geosci. Remote Sens.*, vol. 49, no. 10, pp. 3582–3592, Oct. 2011.

[12] M. J. Rouault, A. Mouche, F. Collard, J. A. Johannessen, and B. Chapron, "Mapping the Agulhas Current from space: An assessment of ASAR surface current velocities," *J. Geophys. Res., Oceans*, vol. 115, no. C10, 2010, Art. no. C10026.

[13] M. W. Hansen, J. A. Johannessen, K. F. Dagestad, F. Collard, and B. Chapron, "Monitoring the surface inflow of Atlantic Water to the Norwegian Sea using Envisat ASAR," *J. Geophys. Res., Oceans*, vol. 116, no. C12, 2011, Art. no. C12008.

[14] G. Engen, H. Johnsen, and Y. Larsen, "Sentinel-1 geophysical Doppler product - Performance and application," in *Proc. 10th Eur. Conf. Synthetic Aperture Radar*, 2014, pp. 1–4.

[15] H. Johnsen, V. Nilsen, G. Engen, A. Mouche, and F. Collard, "Ocean Doppler anomaly and ocean surface current from Sentinel-1 TOPS mode," in *Proc. IEEE Int. Geosci. Remote Sens. Symp.*, 2016, pp. 3993–3996.

[16] M. Rodriguez-Cassola *et al.*, "Doppler-related distortions in TOPS SAR images," *IEEE Trans. Geosci. Remote Sens.*, vol. 53, no. 1, pp. 25–35, Jan. 2015.

[17] G. Hajduch *et al.*, "Sentinel-1 A and B annual performance report for 2020," Tech. Rep. MPC-0504, 2021. [Online]. Available: https://sentinel.esa.int/documents/247904/4607145/Sentinel-1-Annual-Performance-Report-2020.pdf/1eac12a7-26ca-002c-b3ff-78f6a1d77653

[18] A. Elyouncha, L. E. B. Eriksson, H. Johnsen, and L. M. H. Ulander, "Using Sentinel-1 ocean data for mapping sea surface currents along the Southern Norwegian coast," in *Proc. IEEE Int. Geosci. Remote Sens. Symp.*, 2019, pp. 8058–8061.

[19] A. Moiseev, H. Johnsen, M. W. Hansen, and J. A. Johannessen, "Evaluation of radial ocean surface currents derived from Sentinel-1 IW Doppler shift using coastal radar and Lagrangian surface drifter observations," *J. Geophys. Res., Oceans*, vol. 125, no. 4, 2020, Art. no. e15743.

[20] R. Romeiser and D. R. Thompson, "Numerical study on the along-track interferometric radar imaging mechanism of oceanic surface currents," *IEEE Trans. Geosci. Remote Sens.*, vol. 38, no. 1, pp. 446–458, Jan.2000.

[21] M. Hansen *et al.*, "Simulation of radar backscatter and Doppler shifts of wave current interaction in the presence of strong tidal current," *Remote Sens. Environ.*, vol. 120, pp. 113–122, 2012.

[22] Y. Yurovsky, V. Kudryavtsev, S. Grodsky, and B. Chapron, "Sea surface Ka-band Doppler measurements: Analysis and model development," *Remote Sens.*, vol. 11, no. 7, p. 839, Apr. 2019.

[23] A. Elyouncha, L. E. B. Eriksson, R. Romeiser, and L. M. H. Ulander, "Empirical relationship between the Doppler centroid derived from X-band spaceborne InSAR data and wind vectors," *IEEE Trans. Geosci. Remote Sens.*, vol. 60, pp. 1–20, 2022.

[24] A. C. H. Martin, C. Gommenginger, J. Marquez, S. Doody, V. Navarro, and C. Buck, "Wind-wave-induced velocity in ATI-SAR ocean surface currents: First experimental evidence from an airborne campaign," *J. Geophys. Res., Oceans*, vol. 121, no. 3, pp. 1640–1653, 2016.

[25] ESA, "Sentinel-1 product definition," document S1-RS-MDA-52-7440, 2016, https://sentinel.esa.int/documents/247904/1877131/Sentinel-1-Product-Definition
[26] M. Zink *et al.*, "TanDEM-X: 10 years of formation flying bistatic SAR interferometry," *IEEE J. Sel. Topics Appl. Earth Observ. Remote Sens.*, vol. 14, pp. 3546–3565, 2021.
[27] P. A. Hwang, W. J. Teague, G. A. Jacobs, and D. W. Wang, "A statistical comparison of wind speed, wave height, and wave period derived from satellite altimeters and ocean buoys in the Gulf of Mexico region," *J. Geophys. Res., Oceans*, vol. 103, no. C5, pp. 10451–10468, 1998.
[28] A. Moiseev, H. Johnsen, J. A. Johannessen, F. Collard, and G. Guitton, "On removal of sea state contribution to Sentinel-1 Doppler shift for retrieving reliable ocean surface current," *J. Geophys. Res., Oceans*, vol. 125, no. 9, 2020, Art. no. e2020JC016288.
[29] H. C. Graber, D. R. Thompson, and R. E. Carande, "Ocean surface features and currents measured with synthetic aperture radar interferometry and HF radar," *J. Geophys. Res.*, vol. 101, no. C11, pp. 25813–25832, Nov. 1996.
[30] R. F. Hanssen, *Radar Interferometry: Data Interpretation and Error Analysis*, 1st ed. Berlin, Germany: Springer, 2001.
[31] S. Draper, T. A. A. Adcock, A. G. Borthwick, and G. T. Houlsby, "Estimate of the tidal stream power resource of the Pentland Firth," *Renewable Energy*, vol. 63, pp. 650–657, 2014.
[32] M. Tonani *et al.*, "The impact of a new high-resolution ocean model on the met office North-West European Shelf forecasting system," *Ocean Sci.*, vol. 15, no. 4, pp. 1133–1158, 2019.
[33] A. Mouche *et al.*, "On the use of Doppler shift for sea surface wind retrieval from SAR," *IEEE Trans. Geosci. Remote Sens.*, vol. 50, no. 7, pp. 2901–2909, Jul. 2012.

Anis Elyouncha (Member, IEEE) received the M.S. degree in electrical engineering and telecommunications from the Universite Libre de Bruxelles, Brussels, Belgium, in 2006, and the Ph.D. degree in radio and space sciences from the Chalmers University of Technology, Gothenburg, Sweden, in 2020.

From 2008 to 2015 he was a Research Engineer with the Royal Military Academy of Belgium. He is currently a Postdoctoral Researcher with the Department of Space Earth and Environment, Chalmers University of Technology. His research interests include ocean parameters retrieval from SAR data, electromagnetic scattering from the sea surface, and radar signal processing.

Leif E. B. Eriksson (Member, IEEE) received the University Certificate in space technology from Umeå University, Umeå, Sweden, in 1993, the M.S. degree in electrical engineering from the Chalmers University of Technology, Gothenburg, Sweden, in 1998, and the Ph.D. degree in natural sciences from Friedrich-Schiller University, Jena, Germany, in 2004.

From 1999 to 2000, he was employed by the Joint Research Centre of the European Commission, Space Application Institute in Ispra, Italy, between 2000 and 2004, he was with the Department of Geoinformatics, Friedrich-Schiller University, Jena, Germany, In 2004, he joined the radar remote sensing group at the Chalmers University of Technology, where he has been an Associate Professor of radar remote sensing since 2012, and is currently with the Department of Space, Earth and Environment. His research interests include the use of SAR to retrieve information about ocean, sea ice, and forest.

Harald Johnsen (Member, IEEE) received the M.Sc. and Ph.D. degrees in experimental plasma physics from the University of Tromsø, Tromsø, Norway, in 1981 and 1984, respectively.

He was with the Auroral Observatory, Tromsø for two years. He was a Research Scientist with the Earth Observation Group, Norut IT, Tromsø from 1986 until 2019 when he joined NORCE – Norwegian Research Center as Chief Scientist. He is currently an Associate Professor with UiT – The Arctic University of Norway, Troms, Norway. His research interests include SAR ocean applications and SAR interferometry applications.